



HAL
open science

High-resolution surface wave tomography beneath the Aegean-Anatolia region: constraints on upper-mantle structure

Gwénaëlle Salaun, Helle Pedersen, Anne Paul, Véronique Farra, Hayrullah Karabulut, Denis Hatzfeld, Costas Papazachos, Dean M Childs, Catherine Péquegnat

► To cite this version:

Gwénaëlle Salaun, Helle Pedersen, Anne Paul, Véronique Farra, Hayrullah Karabulut, et al.. High-resolution surface wave tomography beneath the Aegean-Anatolia region: constraints on upper-mantle structure. *Geophysical Journal International*, 2012, 190 (1), pp.406-420. 10.1111/j.1365-246X.2012.05483.x . hal-02156801

HAL Id: hal-02156801

<https://hal.science/hal-02156801v1>

Submitted on 14 Jun 2019

HAL is a multi-disciplinary open access archive for the deposit and dissemination of scientific research documents, whether they are published or not. The documents may come from teaching and research institutions in France or abroad, or from public or private research centers.

L'archive ouverte pluridisciplinaire **HAL**, est destinée au dépôt et à la diffusion de documents scientifiques de niveau recherche, publiés ou non, émanant des établissements d'enseignement et de recherche français ou étrangers, des laboratoires publics ou privés.

High-resolution surface wave tomography beneath the Aegean-Anatolia region: constraints on upper-mantle structure

Gwénaëlle Salaün,¹ Helle A. Pedersen,¹ Anne Paul,¹ Véronique Farra,² Hayrullah Karabulut,³ Denis Hatzfeld,¹ Costas Papazachos,⁴ Dean M. Childs,³ Catherine Pequegnat¹ and SIMBAAD Team*

¹Institut des Sciences de la Terre, Université de Grenoble 1, CNRS, F-38041 Grenoble, France. E-mail : anne.paul@obs.ujf-grenoble.fr

²Institut de Physique du Globe de Paris, Paris, France

³Kandilli Observatory and Earthquake Research Institute, Bogaziçi University, Istanbul, Turkey

⁴Department of Geophysics, Aristotle University, Thessaloniki, Greece

Accepted 2012 March 27. Received 2012 March 15; in original form 2011 June 16

SUMMARY

This study provides new constraints on the upper-mantle structure from western Greece to central Anatolia using seismic data of permanent broad-band networks recently installed in Greece and Turkey and from a two-year temporary array (SIMBAAD experiment). We used ~200 seismic events recorded at 146 broad-band stations with a typical interstation distance of 60–100 km across the study area. The high-resolution 3-D shear wave velocity model of the mantle is obtained by inversion of fundamental-mode Rayleigh wave phase velocity maps for periods between 20 and 195 s. The tomography is based on ray tracing in heterogeneous media taking into account external propagation effects. The horizontal resolution is approximately 100 km, however small heterogeneities may suffer from some horizontal smearing and damping. The vertical resolution is approximately 100 km. The vertical smoothing is necessary to avoid unresolved spurious shear wave velocity oscillations in the upper mantle. The errors on shear wave velocities in our 3-D model (0.02–0.1 km s⁻¹) are significantly smaller than the amplitude of V_s variations (0.3–0.5 km s⁻¹). In spite of the vertical and horizontal smoothing, our model shows details in the upper-mantle structure never reached at regional scale in the area. The overall structure is characterized by a low-velocity zone (80–200 km depth) reflecting a slow and warm asthenosphere underlying a thin lithosphere. The southwesternmost termination of the low-velocity anomaly corresponds to the northward dipping Hellenic slab. The detailed shear velocity structure of the upper mantle beneath Anatolia appears to be far more geometrically complex than revealed in previous tomographic studies of the area. At depths larger than or equal to 160 km, velocities are overall high beneath Anatolia, partly due to the presence of dipping high-velocity anomalies which we tentatively interpret as remnant slabs. The southernmost high-velocity anomaly beneath Anatolia is separated from the eastern edge of the Hellenic slab by a major low-velocity anomaly which we interpret as the trace of asthenospheric mantle material rising inside a vertical slab tear beneath southwestern Anatolia.

Key words: Surface waves and free oscillations; Seismic tomography; Continental tectonics; compressional; Dynamics of lithosphere and mantle; Europe.

*SIMBAAD Team: T. Afacan and M. Aktar (Kandilli Observatory and Earthquake Research Institute, Bogaziçi University, Istanbul, Turkey), E. Bourova-Flin (Institut des Sciences de la Terre, Université de Grenoble 1, CNRS, F-38041 Grenoble, France), D. Cambaz (Kandilli Observatory and Earthquake Research Institute, Bogaziçi University, Istanbul, Turkey), P. Hatzidimitriou (Department of Geophysics, Aristotle University, Thessaloniki, Greece), F. Hubans (Institut des Sciences de la Terre, Université

de Grenoble 1, CNRS, F-38041 Grenoble, France), D. Kementzetzidou, E. Karagianni and I. Karagianni (Department of Geophysics, Aristotle University, Thessaloniki, Greece), A. Komec Mutlu (Kandilli Observatory and Earthquake Research Institute, Bogaziçi University, Istanbul, Turkey), L. Dimitrova (Bulgarian Academy of Science, Sofia, Bulgaria), Y. Ozakin (Kandilli Observatory and Earthquake Research Institute, Bogaziçi University, Istanbul, Turkey), S. Roussel (Institut des Sciences de la Terre,

1 INTRODUCTION

The eastern Mediterranean is a complex and rapidly deforming region for which present-day mantle dynamics and its contribution to surface deformation, kinematics and dynamic topography are only partly understood. For example, the relative contribution of different processes such as Africa–Eurasia convergence, large- and small-scale upper-mantle convection, Hellenic slab retreat and westward motion of Anatolia, remains poorly understood. A coherent picture is slowly emerging for the Aegean for which many geological and geophysical data are available, but further progress is prohibited by the lack of knowledge of upper-mantle structures beneath Anatolia.

Providing high-resolution seismic constraints and more uniform information on mantle structure beneath the broad area including Continental Greece, the Aegean Sea and western and central Anatolia is the goal of this work. We use data from temporary and permanent seismic stations throughout the study region to investigate the absolute shear velocity from 80 to 300 km depth by surface wave tomography.

Surface wave tomography has the advantage of a good compromise between vertical and horizontal resolutions as compared to teleseismic body wave tomography; the latter has excellent horizontal resolution but suffers from vertical smearing and an unknown background velocity model. Intermediate to long-period single- or multi-mode surface wave tomography is however far from straightforward. All along their paths between source and receiver, intermediate period surface waves sample a medium which is strongly heterogeneous at all wavelengths. Using simplistic approximations in the data analysis is therefore not justified, but the difficulties are such that no single method presently available addresses all of the main difficulties.

In the case of large-scale studies where the seismic sources and sensors are located inside the study area, higher modes, full waveform modelling and diffraction can be taken into account (e.g. Maupin 1988, Snieder 1988; Nolet 1990; van der Lee & Nolet 1997; Debayle 1999; Yoshizawa & Kennett 2002; Lebedev *et al.* 2005; Fichtner *et al.* 2008). Beneath dense seismic arrays with sources located outside the study area, it is possible to obtain better resolution than for larger scale studies, but the set of problems to address is partly different. One specific problem is that the wave train analysed is dominated by propagation effects outside the array. It has so far, in practice, been feasible to work mainly on fundamental mode surface waves as the higher modes can be extracted only under some restrictive conditions (e.g. Beucler *et al.* 2003). Deviations from great-circle propagation can be significant for most of the period range considered in lithospheric studies (e.g. Cotte *et al.* 2000). This may introduce significant errors in local phase velocity estimates. Propagation effects outside the array may introduce significant distortions in the wave fronts which can produce errors in local phase estimates (Friederich *et al.* 1994). Many surface wave studies using teleseismic events and dense arrays still remain based on two-station phase velocity measurements under the assumption of great-circle propagation. Such two-station methods are relatively robust if wave diffraction outside the array is random (Pedersen 2006) which may explain the success of this type of study in spite of the very limiting underlying assumptions. The main problem

of classical two-station-based surface wave tomography is that the phase velocity can be measured only along profiles where the seismic source and the two receivers are approximately located on the same great-circle. The number of useable data is therefore greatly reduced. To remedy for this, five main approaches have emerged: (i) representing the full amplitude and phase wavefield in the medium and allowing for non-plane incoming wave fronts (Friederich & Wielandt 1995; Pollitz 1999); (ii) representing the incident wavefield as a sum of two incident plane waves (Forsyth & Li 2005); (iii) estimating the velocity through the gradient of the phase observations in so-called Eikonal tomography (Lin *et al.* 2009); (iv) using finite frequency sensitivity kernels which extend outside the array (Chevrot & Zhao 2007) and (v) ray tracing in a heterogeneous phase velocity model allowing for non-plane incoming wave fronts (Bruneton *et al.* 2002). This latter method provided very similar results (Friederich, personal communication, 2004) to the method of Friederich & Wielandt (1995) in the case of a 3-D surface wave tomography in the Baltic Shield (Bruneton *et al.* 2004).

A number of large-scale surface and body wave studies in the region provides insight to the overall complexity of the Mediterranean region (e.g. Boschi *et al.* 2004; Marone *et al.* 2004; Chang *et al.* 2010; Schivardi & Morelli 2011). Local body wave tomography (Papazachos & Nolet 1997) and receiver function studies (e.g. Knapmeyer & Harjes 2000; Li *et al.* 2003; Sodoudi *et al.* 2006; Sachpazi *et al.* 2007; Suckale *et al.* 2009) provide local constraints on the crustal and mantle structure locally down to 200 km beneath the Aegean. The teleseismic *P*-wave tomography by Biryol *et al.* (2011) has a good lateral resolution mainly beneath Anatolia. Previous local surface wave studies have been limited by relatively sparse or uneven station coverage. These studies highlight the existence of strong differences in mantle shear velocities in different parts of our study area (Bourova *et al.* 2005; Karagianni *et al.* 2005; Endrun *et al.* 2008; Erduran *et al.* 2008).

No detailed and evenly resolved 3-D model is so far available for the whole of the Aegean-Anatolian area. We here present the 3-D shear wave velocity structure of the uppermost mantle beneath this region from fundamental-mode Rayleigh wave tomography (20–195-s period) based on the analysis of ~200 teleseismic earthquakes recorded at 146 broad-band stations over the region. We use the ray-based surface wave analysis developed by Bruneton *et al.* (2002) which first inverts time delays for local phase velocities, correcting for irregular incoming wave fronts, and secondly inverts these phase velocities to obtain a 3-D shear wave velocity model to 300 km depth. In a complementary paper, we present detailed analysis of the 3-D model and its geodynamic implications.

2 DATA SELECTION AND PROCESSING

The present data set was collected within the framework of the SIMBAAD temporary experiment (Seismic Imaging of the Mantle Beneath the Aegean-Anatolia Domain). The temporary array was installed in the spring of 2007 for 2 yr and designed to fill in the gaps between permanent broad-band stations. The SIMBAAD partners in Turkey (Kandilli Observatory and Earthquake Research Institute, Istanbul) and Greece (Department of Geophysics of Aristotle University of Thessaloniki) provided data recorded at all available broad-band stations of the area in the time period of the SIMBAAD experiment. Additional data from ORFEUS-VEBSN and IRIS-DMC facilities were also analysed. The full data set includes records from 146 broad-band stations belonging to many different networks and with many types of sensors as shown in Fig. 1.

Université de Grenoble 1, CNRS, F-38041 Grenoble, France), M. Scordilis and D. Vamvakaris (Department of Geophysics, Aristotle University, Thessaloniki, Greece).

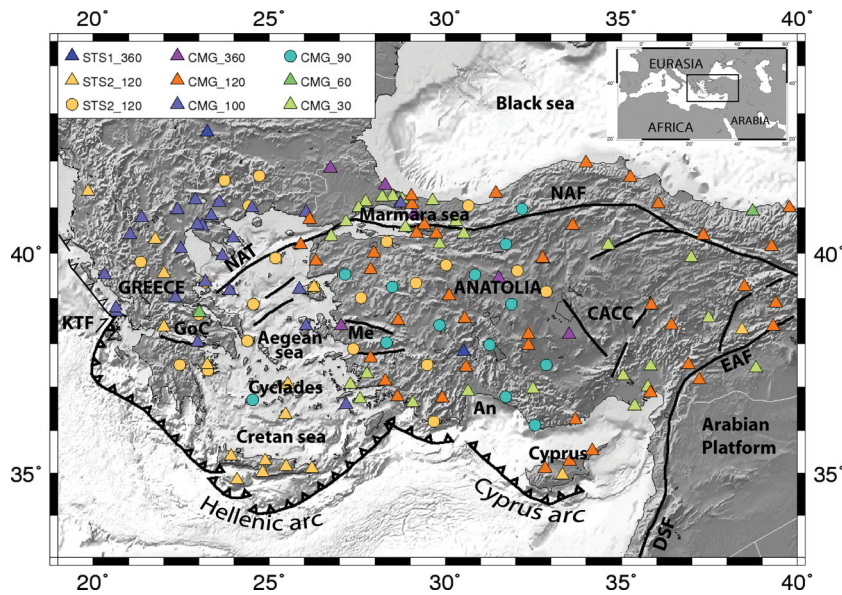


Figure 1. Map of the seismic array used in this study, including temporary (circles) and permanent (triangles) broad-band stations. The colour of markers denotes the type of sensor. In the prefix of the sensor type given in the legend, CMG designates Gralp sensors (CMG3-ESP, CMG3-T, CMG40-T and CMG6-T), and STS2 designates Streckheisen STS-2 sensors. The suffix of the sensor types indicates the cut-off period. Major faults are shown as thick black lines. An, Antalya Bay; CACC, Central Anatolian Crystalline Complex; DSF, Dead Sea Fault; EAF, East Anatolian Fault; GoC, Gulf of Corinth; KTF, Kephalaria Transform Fault; Me, Menderes Massif; NAT, North Aegean Trough; NAF, North Anatolian Fault.

The station coverage is dense (interstation spacing of 60–80 km) in the area [20°E–33°E] and slightly less dense east of 33°E and in the southern Aegean. As shown in Fig. 1, most stations have very broad-band sensors with lower corner frequencies corresponding to periods between 90 and 120 s.

During the 2-yr deployment time of the temporary network, we recorded ~400 teleseismic earthquakes with $M \geq 6$ out of which 198 events (see Fig. 2a) were selected for their high-quality signals. The magnitude 6 threshold was chosen to be able to use the 30 s cut-off period for most events over the whole of the period interval that we use. We specifically verified long-period data quality (similarity of waveforms and similar signal/noise ratio as compared to the other types of sensors) for these stations. The azimuthal coverage is overall good (Fig. 2a) as there are no large gaps in any direction. This good coverage is essential to avoid horizontal direction-dependent smearing and to adequately correct for errors due to leakage of external propagation effects into the array. The number of events from each direction is however unevenly distributed, with a strong dominance of events located east of the array.

After pre-filtering and de-convolving with the instrument responses, the fundamental-mode Rayleigh waves were extracted from the vertical component of the signal using a semi-automatic implementation of a phase-matched filter (Herrin & Goforth 1977; Lander & Levshin 1989). This step ensures the exclusion of other waves and minimizes interferences from higher modes multipathing. We then computed arrival time differences on filtered signals between pairs of stations. For each period and each event, the time delay was obtained through the phase of the Wiener filter (Wiener 1949; Baumont *et al.* 2002; Pedersen *et al.* 2003) between waves recorded at the first station encountered by the wave ('Station 1', used as reference) and the others.

Two-station time delays were measured at periods between 20 and 195 s. The delays associated with a coherence coefficient of more than 0.85 between the two signals in each frequency range were subsequently used in the inversion. Fig. 2(b) shows the number of

time-delay measurements used in the inversion for phase velocities at each period. We obtained a total of 3500–8000 time delays at each period between 20 and 195 s, with a best sampled period at ~120 s, and a total of more than 120 000 measurements.

The main cause of errors in the time delays measured between each station i and station 1 is noise in the seismic signals, which can be very variable between stations. Rather than imposing some constant *ad hoc* error for all stations at a given period, we prefer to estimate some objective error that allows us to identify and associate a higher error to stations with strong noise with the aim at downweighting such measurements in the phase velocity inversion. We base our error estimate on the variability of observed time delays in the area around station i using time delays measured between station 1 and all stations j within a 200 km radius of station i . We subtract from these time delays a theoretical propagation time based on the difference of epicentral distance between stations j and i and the phase velocity from the *ak135* reference model (Kennett *et al.* 1995) at the given frequency, to calculate a 'predicted' time delay at station i , based on the observations from stations j . The uncertainty of the delay measurement ΔT at station i is calculated as the average absolute time difference (L1 norm) between these predicted times and the observed time at station i . Fig. 2(c) shows the error distribution at 180 s period. At all periods, the error distribution can to a first approximation be considered Gaussian ($\exp(-1/2(\Delta T/\sigma)^2)$). σ varies with period, between 0.35 (120 s period) and 0.55 s (180 s period, shown in Fig. 2c). This method does not account for deviations from great-circle propagation and for velocity variations across the area so our predicted times may be slightly wrong, thereby leading to a small overestimation of the error. It could potentially downweight measurements in areas with strong lateral changes in phase velocity, leading to some damping of anomalies. This effect remains small; for example, a 5 per cent velocity variation over 100 km induces an apparent error of 1.3 s. The spatial distributions of the errors on time delays at each period and for each event show no detectable bias created by local heterogeneities. Systematic strong variations

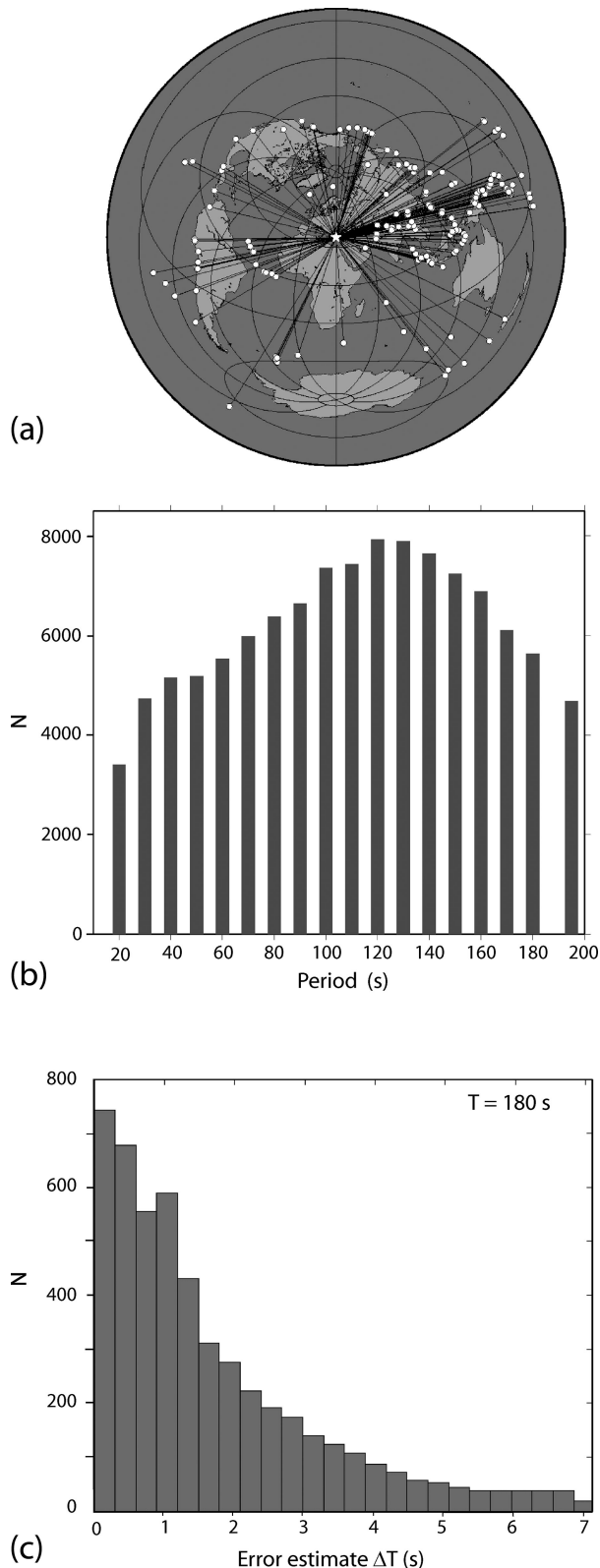


Figure 2. (a) Azimuthal distribution of the 198 earthquakes with $M \geq 6$ used in this study. Epicentres are displayed as white circles, and great-circle paths are traced to the centre of our study area and plotted as black lines. (b) Number of interstation time delays used in the inversion for phase velocity as a function of period. (c) Distribution of the time-delay error estimates at 180 s period.

will therefore be recovered in the inversion so we favour this conservative approach rather than allowing instrumental problems and random errors to create artificial structures inside the model.

3 RAY-BASED INVERSION FOR PHASE VELOCITY MAPS

We first determine 2-D phase velocity variations across our study area for all periods in the range of 20–195 s, that is, for wavelengths between approximately 70 and 900 km. Our array aperture is broad enough (2000×900 km, see Fig. 3) to resolve lateral phase velocity variations to ~ 200 s period, with a lateral resolution which is mainly governed by the interstation distance (e.g. Pedersen *et al.* 2003; Bodin & Maupin 2008). The method consists in inverting the observed delays to obtain phase velocity maps at each period across the array (Bruneton *et al.* 2002). To account for scattering outside the region (Friederich *et al.* 1994), we also invert for the arrival time of the incoming wave fronts at the model edges (Bruneton *et al.* 2002). Note that the inversion, for a given frequency, involves all events, as we simultaneously invert for the shape of the wave front for each event, represented by the arrival times $T_0(X, Y)$ at the edge of the model, and for a unique phase velocity model, represented by the squared slowness $u^2(X, Y)$.

The second step (discussed in Section 5) is to reconstruct, at each gridpoint, a dispersion curve and invert it with an iterative (linear at each iteration) inversion procedure. The collection of 1-D models at all gridpoints constitutes our final 3-D shear wave velocity model. As the methods have been published elsewhere, we here only present the general features, and go into some detail on the parametrization and regularization that we used for the inversions.

3.1 Forward problem and inversion procedure

The iterative inversion procedure implies that we need to calculate, at each iteration, the forward problem, that is, to predict arrival times at all stations for a given phase velocity model and a given incoming wave front. This forward calculation is not trivial, as we need to identify the ray from each station to the edge of the model. The slowness of this ray must at the edge be compatible with the slowness of the incoming wave front, as defined by the spatial derivative (in the direction of the model edge) of the wave front arrival time T_0 . We therefore impose this as a boundary condition of the ray tracing, within some small, acceptable error. The iterative search for the ray satisfying the imposed boundary conditions (for details, see Bruneton *et al.* 2002) is achieved using paraxial ray tracing (Deschamps 1972; Farra & Madariaga 1987). Once the geometry of the ray is obtained, the arrival time of the wave at the receiver is computed by integration along the ray, and adding the arrival time T_0 at the point on the edge where the ray enters the model. Note that the ray tracing is carried out for the actual phase velocity model at each iteration during the inversion procedure.

Practically, T_0 and u^2 are represented by B-spline coefficients (de Boor 1978). Fourth-order 1-D B-splines are used for T_0 whereas third-order 2-D B-splines are used for u^2 . For the two types of parameters, the B-spline coefficients are distributed on grid nodes every 100 km in X and Y -axes oriented towards the east and south, respectively. The number of parameters is dependent on the spatial discretization (N_x, N_y) as it includes ($N_e \times (N_x + N_y)$) parameters to describe the arrival times of the N_e wave fronts at the

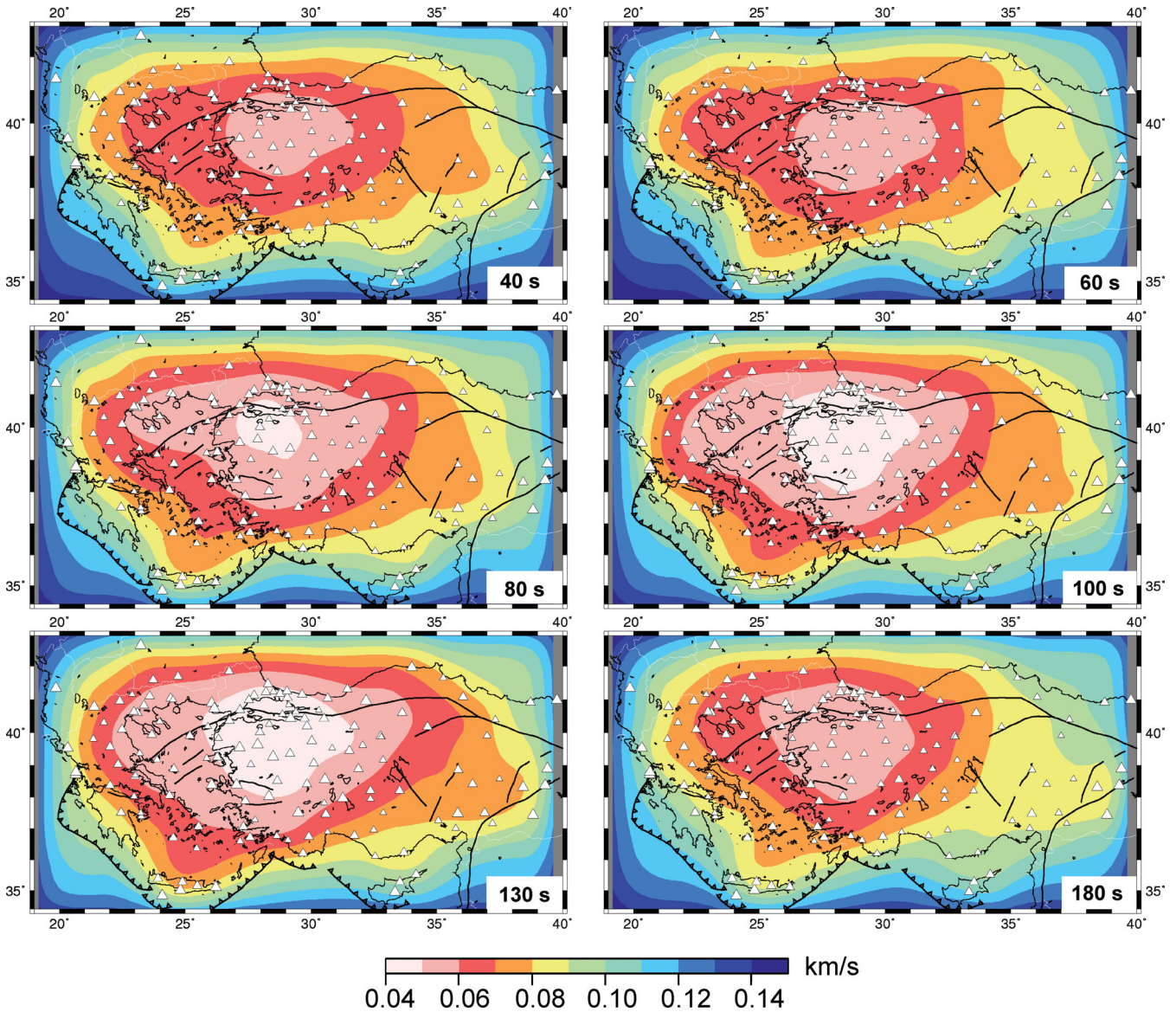


Figure 3. Maps of *a posteriori* error in phase velocity for selected periods. White triangles mark station locations, with size proportional to the number of data used in the inversion.

corresponding model edges and $[(N_x + 1)(N_y + 1)]$ parameters to describe slowness squared in the model. Thus, using a cell size of $100 \text{ km} \times 100 \text{ km}$, we obtain at each period ~ 5750 parameters, which is of the same order as the number of time delays at each period (Fig. 2c). The regularization constraints significantly reduce the number of independent parameters, especially through the smoothing of the incoming wave fronts.

We use a classical inversion procedure (Tarantola 1987) with a misfit function S

$$S(\mathbf{m}) = [\mathbf{T}^{\text{obs}} - \mathbf{T}^{\text{calc}}(\mathbf{m})]^T \mathbf{C}_T^{-1} [\mathbf{T}^{\text{obs}} - \mathbf{T}^{\text{calc}}(\mathbf{m})] + [\mathbf{F}_m - \mathbf{F}(\mathbf{m})]^T \mathbf{C}_F^{-1} [\mathbf{F}_m - \mathbf{F}(\mathbf{m})]$$

where the first term corresponds to data misfit ($\mathbf{T}^{\text{obs}} - \mathbf{T}^{\text{calc}}(\mathbf{m})$) and associated errors (through the introduction of the covariance matrix \mathbf{C}_T), whereas the second term corresponds to a model misfit as compared to *a priori* values (\mathbf{F}_m) of some parameter combinations ($\mathbf{F}(\mathbf{m})$) with associated *a priori* uncertainties (through the *a priori* covariance matrix \mathbf{C}_F) as specified in the following section.

The quadratic approximation of the non-linear least-square misfit function is solved iteratively using a singular value decomposition algorithm. For further details, see Bruneton *et al.* (2002).

3.2 Regularization constraints

Regularization is provided in the form of *a priori* model covariance (Tarantola 1987), which effectively through \mathbf{F}_m smooths the velocity model and the non-plane wave fronts. We control the roughness of the phase velocity model by using *a priori* information on upper limit values of u^2 ($\sigma_{F(u^2)}$) and the first ($\sigma_{F(u^{2'})}$) and second ($\sigma_{F(u^{2''})}$) derivatives of u^2 with regard to the horizontal coordinates. We also impose smoothing of the arrival times T_0 of the incoming non-plane wave front by introducing in the misfit function an *a priori* maximum variation of the spatial derivatives of T_0 ($\sigma_{F(T_0)}$), with respect to the value (in \mathbf{F}_m) obtained for the plane wave incoming with a backazimuth corresponding to great-circle propagation.

The optimal values of these *a priori* constraints ($15 \times 10^{-3} \leq \sigma_{F(u^2)} \leq 25 \times 10^{-3} \text{ s}^2 \text{ km}^{-2}$; $15 \times 10^{-4} \leq \sigma_{F(u^{2'})} \leq 25 \times 10^{-4} \text{ s}^2 \text{ km}^{-3}$; $10 \times 10^{-6} \leq \sigma_{F(u^{2''})} \leq 16 \times 10^{-6} \text{ s}^2 \text{ km}^{-4}$; $\sigma_{F(T_0)} = 5 \times 10^{-2} \text{ s km}^{-1}$) yield the least oscillating model which explains the data adequately, but several combinations are possible as there is a trade-off between the oscillations of the wave fronts represented by T_0 and the oscillations of the slowness squared model u^2 . As pointed out by Pedersen *et al.* (2003) and Bodin & Maupin (2008), local phase velocities of Rayleigh waves can be resolved down to a fraction of the wavelength, the station spacing being the main determining parameter in terms of lateral resolution. We therefore base our regularization constraints on the station geometry for the slowness squared, and on known deviations from great-circle paths for the wave fronts (T_0), as explained later. We carried out numerous tests with these and other values of the constraints to validate them as a good compromise between data fit and model oscillations.

The origin time for each wave front in the initial model is located at the corner of the model upon which the waves theoretically impinge (assuming great-circle propagation), whereas in the real data it is located at the reference station, that is the station first encountered by the wave. As the reference station can be more than 350 km from the corresponding corner, the resulting time-shift can reach 90 s which makes the inversion unstable (Bruneton *et al.* 2002). The first iteration is used to shift by a constant value the arrival time T_0 of the incident wave fronts to obtain $T = 0$ s at the reference station for each event. For this first iteration, we used strong regularization constraints to keep the wave fronts plane and the phase velocity model constant across the array. With the model (T_0, u^2) obtained at this iteration, the predicted time delays and the data are sufficiently close to start the proper inversion process. At each period, the initial model used in the first iteration of the inversion has a homogeneous phase velocity corresponding to the *ak135* model (Kennett *et al.* 1995).

The second iteration is used to retrieve the average phase velocity at each period, which we use as *a priori* velocity for further iterations. Allowed variations around this *a priori* value are chosen between ± 4 and ± 20 per cent, decreasing with period. This choice is based on the results of Curtis *et al.* (1998), who show Rayleigh phase velocity variations of up to 12 per cent at intermediate period (80 s) over the study area. In our regional-scale study and considering our dense station coverage, we expect to be able to retrieve stronger velocity variations. In this iteration and for subsequent ones, we also release the constraints on the geometry of the incoming wave front. The imposed smoothness corresponds, at each edge grid node, to allow for a local deviation from the theoretical backazimuth φ , or, in other terms, to constrain the derivative of the arrival time T_0 of the wave along the boundary according to the relation

$$\partial T_0 / \partial X = -\sin\varphi / c \text{ or } \partial T_0 / \partial Y = -\cos\varphi / c,$$

where c is the phase velocity.

We set this *a priori* maximum allowed variation in T_0' of a wave front ($\sigma_{F(T_0')}$) to 0.05 s km^{-1} , which allows for up to 11° deviation from the theoretical propagation direction φ . This value is chosen as a compromise between too strongly perturbed wave fronts [which can, in principle, perfectly fit the data without any heterogeneous structure inside the study area (Friederich 1998)] and taking into account the effect of the surrounding structure on the distortion of the incoming wavefield. The wave front distortion is period-dependent, but in most cases the azimuthal deviation is less than 10° for most events (e.g. Cotte *et al.* 2000; Alvizuri & Tanimoto

2011; Maupin 2011). Cotte *et al.* (2000) measured deviations of $4\text{--}30^\circ$ over a small array (25 km) in the French Alps at short periods (35 s). They estimated that approximately half of the observed deviations can be accounted for by local deviation due to strong Moho topography while large-scale deviations, such as the one created by the Tibetan Plateau, account for the other half. A value of 11° is therefore a reasonable compromise between taking these large-scale effects into account and avoiding strongly perturbed incoming wave fronts. If we allow for a higher angle [i.e. larger variation of the arrival times derivatives of the incoming wave fronts ($\sigma_{F(T_0')}$)], the wave fronts parameters would strongly dominate the inversion.

From the third iteration and onwards, we control the degree of roughness of u^2 mainly by constraining the first and second derivatives of u^2 to be zero with *a priori* uncertainties $\sigma_{F(u^{2'})}$ and $\sigma_{F(u^{2''})}$, respectively. There is a simple link between the *a priori* uncertainty $\sigma_{F(u^{2'})}$ applied to the first derivative ($u^{2'}$) of the squared slowness, and the corresponding constraint $\sigma_{F(c')}$ on the first derivative c' of the phase velocity c

$$\sigma_{F(u^{2'})} = \frac{2}{c^3} \sigma_{F(c')}.$$

In the final iteration, we use $\sigma_{F(u^{2'})} = 0.0003 \text{ s}^2 \text{ km}^{-3}$, which corresponds to a 5 per cent variation of c over a distance of 20 km, if we approximate the phase velocity as 4 km s^{-1} . Finite difference considerations imply that the *a priori* uncertainty $\sigma_{F(u^{2''})}$ should be equal to $2 \sigma_{F(u^{2'})} / dX$, where dX is the distance between two adjacent nodes (in our case 100 km). The two constraints are somewhat redundant, but the *a priori* uncertainty on the second derivative helps in practice to avoid spurious oscillations of the squared slowness u^2 .

At most periods, the data misfits associated with the final models are generally obtained after four iterations and correspond to a decrease of 42–52 per cent as compared to the data misfit computed for the model obtained at the second iteration.

4 RESOLUTION ASSESSMENT AND PHASE VELOCITY MAPS

In the inversion for phase velocity maps, the *a posteriori* covariance matrix of the model is computed following Tarantola (1987). The *a posteriori* error σ_c on phase velocity c can be computed by

$$\sigma_c = \left(\frac{c^3}{2} \right) \sigma_{u^2},$$

where σ_{u^2} is the *a posteriori* error on u^2 . To avoid a period-dependent factor of σ_c (due to the changes in average phase velocity with period) when we apply identical *a priori* constraints, we use a constant value (4 km s^{-1}) of c to obtain comparable values of the *a posteriori* error σ_c . In the inversion procedure, after converging towards the best model, we compute the *a posteriori* errors on parameters (u^2 and T_0) for this model. We use the same *a priori* covariance matrix for all periods, first to compare models obtained with the same number of independent parameters, and second to compare the spatial distribution of the *a posteriori* errors at different periods. In this case, the imposed *a priori* uncertainty on phase velocity (0.15 km s^{-1}) corresponds to the upper bound of the *a posteriori* error below which data carry information about the phase velocity model.

Fig. 3 shows maps of the *a posteriori* error in phase velocity for periods between 40 and 180 s. For the period range 20–195 s, the

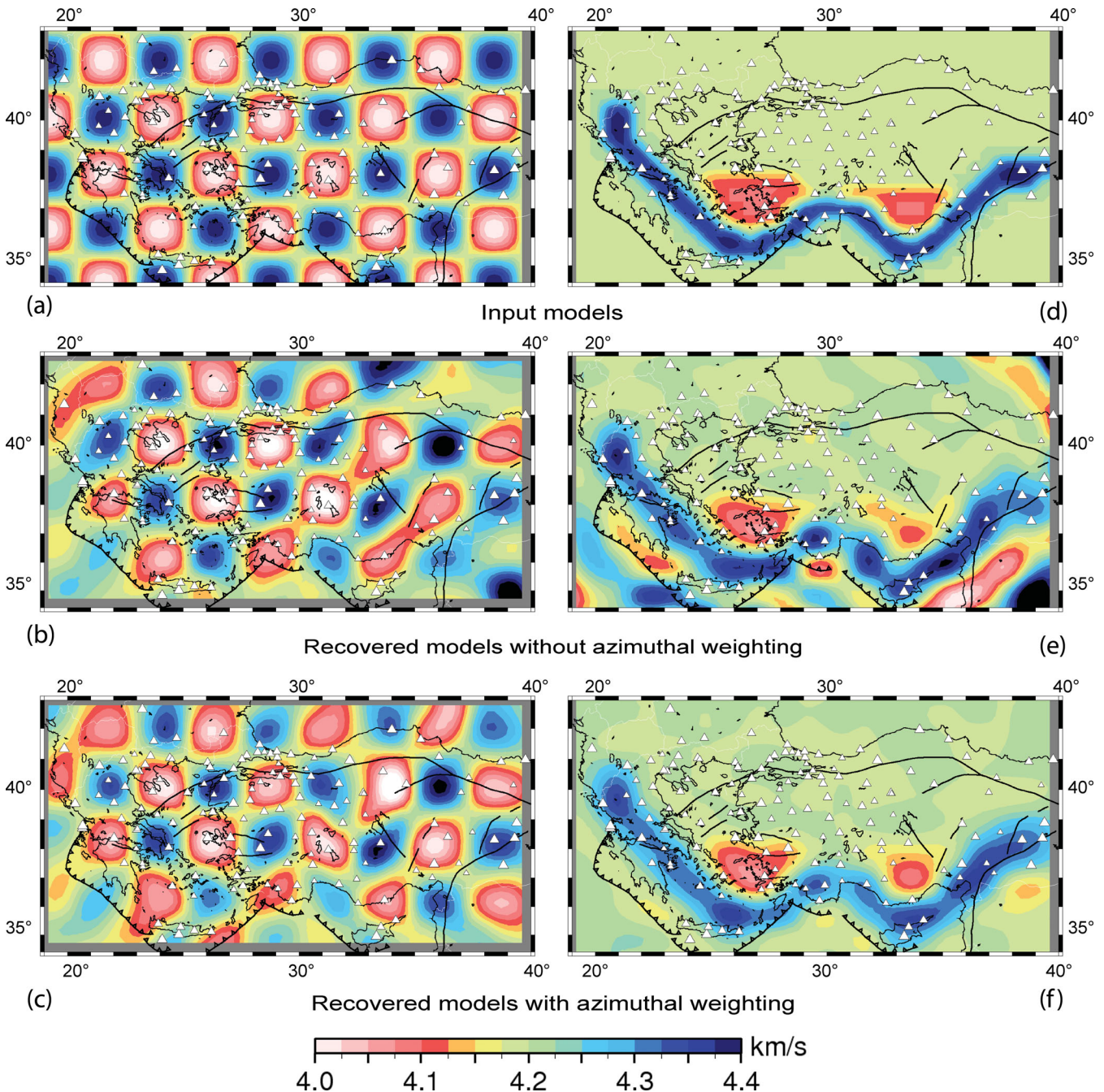


Figure 4. Examples of resolution tests. The distribution of stations and events exactly mimics our data set at 120 s period. (a) and (d) show the input velocity models. (a)–(c) checkerboard test with 200-km anomalies. (d)–(f): High-velocity anomalies 50–100 km wide mimicking subducting slabs north of the Hellenic and Cyprus trenches. (b) and (e) show the recovered phase velocity anomalies after inversion of the synthetic time delays with added random noise. (c) and (f) show the recovered anomalies when time-delay observations are weighted to overcome the uneven distribution in backazimuth (see text).

a posteriori error in the region covered by stations is lower than 0.11 km s^{-1} , which corresponds to an error in phase velocity of 2.75 per cent. This error drops to a minimum of 1 per cent in the centre of the array. These error maps show that model parameters are well resolved across the array in general, but that some caution must be taken when interpreting anomalies on the edges of the model.

The first series of synthetic resolution tests were conducted on checkerboard models of various anomaly sizes. Figs 4(a)–(c) show the test with 200 km wide anomalies, using our real data distribution at 120 s. As illustrated by the *a posteriori* error (Fig. 3), the effective

path distribution at other periods is such that the checkerboard result is stable for a wide range of periods. Even at long period, where the *a posteriori* error increases in the eastern part of the model, the inversion remains stable (see Fig. S1 in the Supporting Information for checkerboard test at 180 s period). The cells used in the inversion are translated 30 km northwards relative to the centre of each velocity anomaly in the checkerboard to verify that model recovery is not dependent on amplitude anomalies being located precisely in the centre of each cell. To use a conservative estimate of data errors, we introduce Gaussian random noise with $\sigma = 0.55 \text{ s}$, as observed in our field data at 180 s period (see Fig. 2c).

The result of the inversion (Fig. 4b) shows that the anomalies are overall well retrieved, both in geometry and amplitude. The model strongly deteriorates as soon as the station coverage becomes poor, towards the edge of the model. Some smearing in the NE–SW direction is present in most areas except in the parts of the area where station density is highest. The smearing inside the model is caused by the dominance of seismic events from E and NE. Fig. 4(c) shows the result of the inversion where we apply azimuthal weighting of the data using the inverse of the square root of the number of events over a 30° wide backazimuth window. The azimuthal weighting effectively reduces smearing both in the centre and at the edges of the model.

Checkerboard models are insufficient to fully assess the resolution of the inversion. The location of the stations inside the model does however minimize this problem as compared to teleseismic body wave tomography (e.g. Lévêque *et al.* (1993)). One of the main aims of this study is to image a high-velocity anomaly associated with the Hellenic slab and its possible continuation towards Cyprus. Figs 4(d)–(f) show the result of an inversion with a continuous high-velocity anomaly north of the trench across the whole model. Two low-velocity anomalies which could mimic low velocities due to a mantle wedge are located immediately north of the high-velocity anomaly. The high-velocity anomaly (+0.2 km s⁻¹; i.e. ~4 per cent) is approximately 80 km wide to test to which degree the lateral smoothing that we impose in the inversion widens the anomaly in the recovered model. Due to the geometry of the high-velocity anomaly, the smearing due to uneven azimuthal distribution (Fig. 4e) is minimal, but the eastern low-velocity anomaly is reduced in size and amplitude. Artificial and strong oscillations are present outside the array. The azimuthal weighting considerably improves the resulting model outside the array and, more importantly, the eastern low-velocity anomaly is much better retrieved. As expected, the width of the high-velocity anomaly is increased and the amplitude is reduced up to 0.1 km s⁻¹ (~2 per cent), and in most places approximately 0.05 km s⁻¹. The smoothing therefore leads to potentially underestimated phase velocity variations for narrow structures. The recovered high-velocity anomaly varies in amplitude along the slab, in particular it is reduced in the areas closest to the edge of the array. These resolution problems do however not create artificial large-scale slab windows.

As the slab is not vertical, its location is period-dependent. At long periods, the phase velocity anomaly will be located further north, that is be shifted towards the centre of the model, where the resolution is even better. At shorter periods, it would shift southwards, and approach the edge of the area covered by seismic stations. Inspired by the result of the inversion of observed time delays (see below) we also need to test the presence of a hole in the high-velocity anomaly, located in southwestern Anatolia. Including these two features in the model (see Fig. S1 in the Supporting Information) shows that the hole is recovered as it is located in a reasonably well-resolved area. The slab geometry and amplitude is more poorly recovered towards the edge of the array. For example, the apparent continuity of the slab is created by lateral smoothing and lack of stations at sea. We have based the discussion only on well-resolved areas.

The phase velocity maps at selected periods are shown in Fig. 5. In this figure, we observe numerous small-scale (~200-km size) phase velocity anomalies and we will concentrate our description on velocity features coherently imaged at nearby periods showing robust and reliable structures. From 40 to 80 s of period, most of Anatolia (south of NAF and North of EAF) is characterized by low-velocity anomalies (-5 per cent ≤ $\delta c/c$ ≤ -3.75 per cent). Within the low-velocity anomalies, those observed beneath south-

western Anatolia are spatially coherent from 40 to 160 s of period and those present between the Antalya Bay and Cyprus show strong amplitude (~ -5 per cent) at long periods (≥100 s). At periods shorter than 100 s, a continuous high-velocity anomaly (~7 per cent) is observed in western Greece. High-velocity anomalies are also found in the southern part of the Aegean Sea. At periods larger or equal to 100 s, a high-velocity anomaly (~3 per cent) appears in the northern part of central Anatolia (~31–37°E, north of 38°N).

5 INVERSION FOR 3-D SHEAR WAVE VELOCITY MODEL

5.1 Method

To image the shear velocity structure in the mantle, we inverted the phase velocity dispersion curves measured at each cell (25 km × 25 km after B-spline interpolation of the phase velocity maps) for 1-D *S*-wave velocity profiles. We use the linear method of Maupin & Cara (1992), which is based on the inversion algorithm of Tarantola & Valette (1982), and iterate over five steps to invert the dispersion curves. The parametrization makes it possible to handle both independent layers and continuously varying velocities between any given pair of interfaces. Following the inversion procedure by Maupin & Cara (1992), only *S*-wave velocity is set free. *P*-wave velocity, density and depth of the interfaces are kept constant. The number of parameters is given by the number of points used to discretize the model with depth (here 332). However, the inversion is not dependent on the model discretization with depth but only on *a priori* information: the vertical correlation length and the *a priori* variance of *S*-wave velocity. To calculate the phase velocities in a spherically symmetric model and their partial derivatives, we used the program package of Saito (1988). In the *a priori* covariance matrix, the correlation length defines the smoothness of the shear wave velocity variations with depth. We choose the longest correlation length (100 km) that adequately explains the local dispersion curves, and use this correlation length as a proxy for vertical resolution.

The crustal structure cannot be well constrained by our dispersion curves as we only use periods greater than 20 s. Moreover, the crustal thickness has strong influence on phase velocity dispersion at intermediate periods. The Moho depth is thus a key input parameter in the inversion process for reliable *V_s* models for the mantle. We used the Moho depth map computed by Hubans (2010) from ambient noise tomography using the same seismic stations as in this study which is the most accurate model of crustal thickness for our study region and covers a large part of it. For areas that are not covered by the model of Hubans (2010) (e.g. the Black Sea region, southwestern Aegean), we used the EuCRUST-07 model of Tesauro *et al.* (2008) which, of several available models (e.g. Mooney *et al.* 1998; Grad *et al.* 2009), is the one which is the closest to Hubans's model in the areas where they overlap. The crustal model of Hubans (2010) is in good agreement with the Moho depth maps of Sodoudi *et al.* (2006), Karagianni & Papazachos (2007) and Tirel *et al.* (2004) beneath the Aegean Sea. It is also in good agreement with known crustal thicknesses beneath the Marmara Sea, as obtained by Bécél *et al.* (2009). Receiver functions from dense north–south profiles in Anatolia (Karabulut *et al.* 2010) show Moho depths that are similar within 2–4 km to the model of Hubans. We carried out a series of synthetic tests that show that our inversion process for shear wave velocity is sensitive to small crustal thickness errors from depths directly below

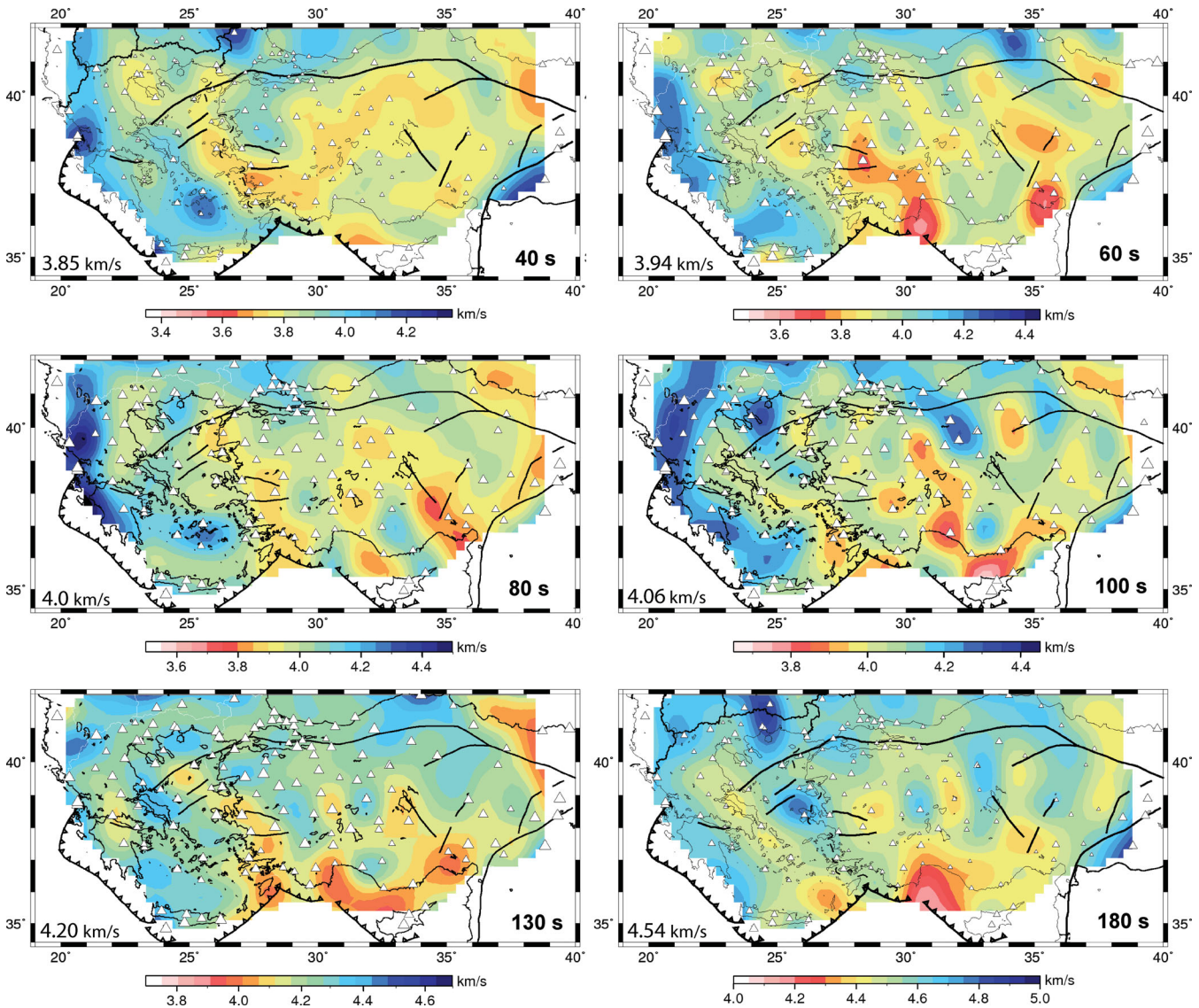


Figure 5. Phase velocity maps at selected periods. Note that the colour scale changes with period, with green corresponding to the average phase velocity as given in the lower left corner of each map. Station locations are shown as white triangles, with size proportional to the number of data used in the inversion.

the Moho to approximately 80 km depth, below which the leaking of the error becomes negligible.

5.2 Average V_s structure and examples of 1-D profiles

Fig. 6(a) shows the average Rayleigh wave phase velocity dispersion curve across the whole study area and two dispersion curves which exemplify the strong lateral variations that we observe. The dispersion curve corresponding to the *ak135* earth model (Kennett *et al.* 1995) is added for reference. The *ak135* V_s model and the result of the inversion of the average and the two examples of dispersion curves, and the associated errors in V_s are shown in Fig. 6(b). Note that the errors are small down to 300 km depth which we consider as the maximum depth of our 3-D model.

The average phase velocities between 30 and 150 s period across the area are slow as compared to *ak135*. These low phase velocities translate into low upper-mantle velocities down to 220 km depth, most notably between 125 and 175 km depth where average V_s is

4.5–5 per cent lower than *ak135*. Low velocities at large scale are also observed in other recent regional (Marone *et al.* 2004; Maggi & Priestley 2005; Chang *et al.* 2010) and global (Debayle *et al.* 2005) S -velocity models below the bulk of our study area (Anatolia and Aegean Sea) with a similar maximum amplitude relative to *ak135*.

Previous local seismological studies of the area have largely focused on the Aegean Sea. It is therefore possible to compare our results to those of previous studies through the example location in the Cretan Sea (blue). At this point, the crustal model that we use (Hubans 2010) has a Moho at 27 km depth, which is close to values obtained by Sodoudi *et al.* (2006) (25–28.5 km) from receiver functions and Karagianni & Papazachos (2007) (28–32 km) from regional surface wave analysis. The surface wave study by Karagianni & Papazachos (2007) has very limited resolution below Moho as they obtained dispersion curves between 5 and 27 s period. They did however show some indication of a thin (10–15 km thick) layer of low V_s immediately below Moho. This result is in agreement with those of Endrun *et al.* (2008) who have limited path coverage but who extract phase velocity dispersion up to 200 s

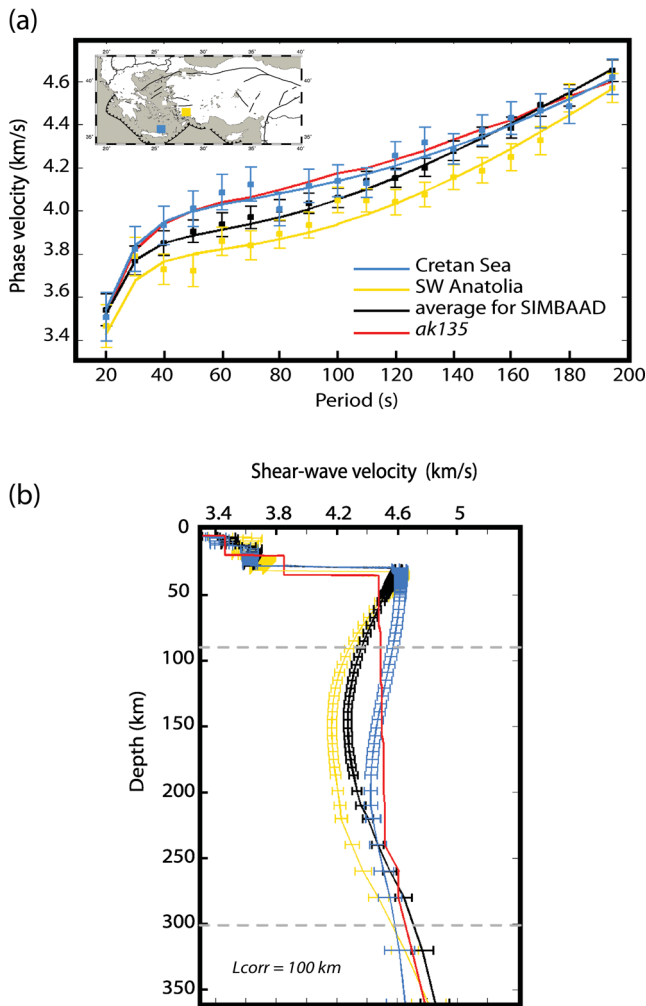


Figure 6. Results of the inversion of Rayleigh wave phase velocity dispersion curves (a) for 1-D V_s models (b) at selected locations shown in the map in inset. Symbols in (a) correspond to phase velocities data shown in Fig. 5 and dispersion curves of the obtained $V_s(Z)$ models are shown as lines. Error bars in (a) show the *a posteriori* errors in phase velocity taken into account in the inversion for V_s models. Phase velocities and shear wave model for *ak135* (Kennett *et al.* 1995) are shown in red. The dotted thin grey lines in (b) indicate the depth range where the V_s model is resolved (80–300 km). L_{corr} is the vertical correlation length used in the inversion for V_s .

in the Cretan Sea. Conversely, our results and other surface wave studies in the area did not highlight low group or phase velocities which would be indicative of a mantle wedge (Bourova *et al.* 2005; Cambaz & Karabulut 2010) between Crete and the Cyclades. Mutlu & Karabulut (2011), who studied P_n propagation beneath the same array as in this study, did also not identify very low velocities along the volcanic arc.

Our results for the point in the Cretan Sea do not show low velocities beneath Moho. This difference with the results obtained by Endrun *et al.* (2008) can be explained by our conservative depth smoothing. Our $V_s(Z)$ profile of Fig. 6(b) is indistinguishable, down to 120 km depth, with the $V_s(Z)$ model obtained if we invert the Endrun *et al.* (2008) FODE/IDI-SANT dispersion curve using our chosen correlation length of 100 km. If we invert their dispersion curve with a correlation length of 20 km we obtain a $V_s(Z)$ profile very similar to their proposed model without an overall improvement of the misfit between observed and predicted phase velocities. The

underlying issue of this lack of resolution resides in strong trade-off between crustal structure and uppermost mantle velocities.

As our objective is to study deep structure across the whole of the study area, making sure that we obtain a unique solution with no possibility of non-resolved oscillations with depth, we use a correlation length of 100 km to obtain the 3-D model. This means that thin layers (10–15 km) such as the mantle wedge identified by Papazachos & Nolet (1997), Karagianni *et al.* (2005) and Endrun *et al.* (2008) will not be present in our model.

The differences observed in the 1-D V_s models of Cretan Sea and *ak135* model (Fig. 6b) are mainly caused by differences in Moho depths (8 km shallower for the first one). Such differences in Moho depth, for relatively similar dispersion curves (Fig. 6a), translate into significant differences in mantle velocities down to 120 km depth. However, we estimate the errors on the Moho map to 2–4 km, consequently mantle velocities are not strongly influenced by such errors below 80 km.

The second example is from a point located in SW Anatolia, where velocities in the upper mantle are low down to the bottom of our model, at 300 km depth. The velocities are particularly low, 4.2 km s⁻¹, around 150 km depth. This anomalously slow upper mantle can be explained by the existence of a hot and/or hydrated mantle.

5.3 3-D model and discussion

The 3-D absolute shear wave velocity model obtained by 1-D phase velocity inversions at each gridpoint is illustrated in Fig. 7 as depth slices while the velocity variations with respect to the average model (shown in Fig. 6) can be found in Fig. S2 in the Supporting Information. The relative velocity model is of use because of the horizontal and vertical smoothing which effectively makes it impossible to recover large amplitude variations. A cold high-velocity body embedded in a very slow medium, as we will comment upon below, can therefore not be correctly retrieved as high absolute velocities (see also the discussion on resolution in Section 4). The *a posteriori* error on V_s at each point (X, Y, Z) is recovered from the 1-D inversion (see Fig. 6). The error estimate is shown as depth slices in Fig. S3 in the Supporting Information.

Fig. 7 shows absolute shear wave velocities at 80, 120, 160, 200, 250 and 300 km depth. The depth slice at 50 km depth is shown in Fig. S4 in the Supporting Information, but must be interpreted with caution as there is a strong trade-off between crustal thickness and mantle velocities down to 80 km depth. The colour scale in Fig. 7 is centred on the *ak135* model, where yellow and red show velocities slower than *ak135* while blue colours correspond to velocities higher than *ak135*. With wavelengths λ between 70 and 900 km, we consider that the model is well resolved to depths reaching $\lambda/3$, that is, 300 km. Fig. S3 in the Supporting Information shows the *a posteriori* error on shear wave velocity at selected depths providing information on how the phase velocity uncertainty translates non-linearly into *a posteriori* shear wave velocity uncertainty. At the bottom of our 3-D V_s model, the *a posteriori* error on shear wave velocity is less than 0.1 km s⁻¹ beneath the array.

The main characteristics of the model is the systematic evolution of the velocities from slow at shallower (80–200 km) depths to fast at larger (>200 km) depths as compared to *ak135*. The low velocities extend over almost all of the study area and peak at approximately 120 km depth, with velocities as low as 10 per cent less than *ak135*. Low velocities have also been observed in regional and global surface wave studies (e.g. Marone *et al.* 2004; Debayle

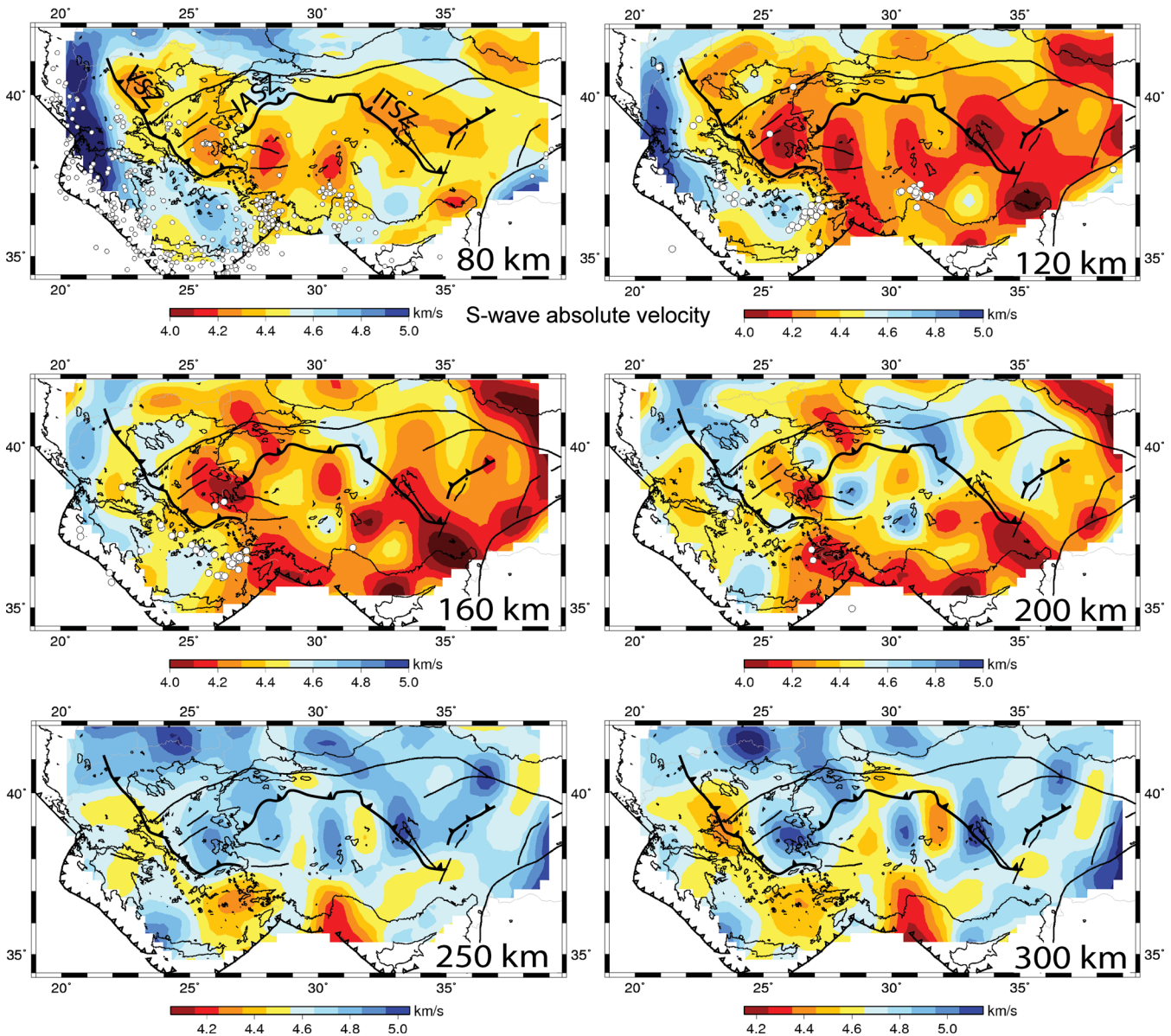


Figure 7. Horizontal slices at selected depths in our absolute 3-D shear wave velocity model. White circles are hypocentres from the 1998–2008 EMSC (Euro-Mediterranean Seismological Centre) catalogue which are located within 10 km of the section depth (except within 5 km at 80 km depth). Major sutures discussed in the text are plotted as thick black lines (from west to east: VSZ for Vardar suture zone; IASZ for Izmir–Ankara suture zone; ITSZ for Inner Tauride suture zone).

et al. 2005; Maggi & Priestley 2005; Chang *et al.* 2010; Schivardi & Morelli 2011) as well as in body wave studies (e.g. Spakman *et al.* 1993; Bijwaard *et al.* 1998; Piromallo & Morelli 2003). The low upper-mantle velocities support a model of lithosphere thinner than 80 km beneath the area, as suggested by Sengör *et al.* (2003) and Angus *et al.* (2006) for eastern Anatolia.

The lateral extension of the low velocities is somewhat less at 80 km depth, where high velocities are identified in the northern and western parts of the model, with small areas of high velocities N–NW of Cyprus. The high velocities in the S–SW part of the model are well explained by the presence of the Hellenic slab. The high velocities along the northern limit of our model at these depths can be explained by the presence of the stable Eurasian lithosphere which is thicker than the lithosphere beneath the Aegean (e.g. Schivardi & Morelli 2011). These high velocities are however limited to small areas as compared to the whole study region.

Below 200 km depth, the model is overall characterized by high velocities, with typical V_s values of 4.7–4.8 km s⁻¹, close to the values inferred by Kustowski *et al.* (2008) beneath the Turkish Plateau, and reaching more than 5 km s⁻¹ at depths >250 km in some areas. Spakman *et al.* (1993) and Piromallo & Morelli (2003) have a similar transition from low to high velocities, albeit located at slightly different depths (approximately 150 and 230 km depth, respectively).

In addition to these very large-scale velocity variations, we obtain a more detailed model than previous authors, in particular beneath Anatolia. Small-scale variations can be identified even though they are embedded in overall low (depths between 80 and 200 km) and high (depth >200 km) velocities. These small-scale velocity variations are significantly larger than the approximately 0.1 km s⁻¹ error on V_s (see Fig. S3 in the Supporting Information). This 3-D small-scale structure is geometrically complex. The complexity of

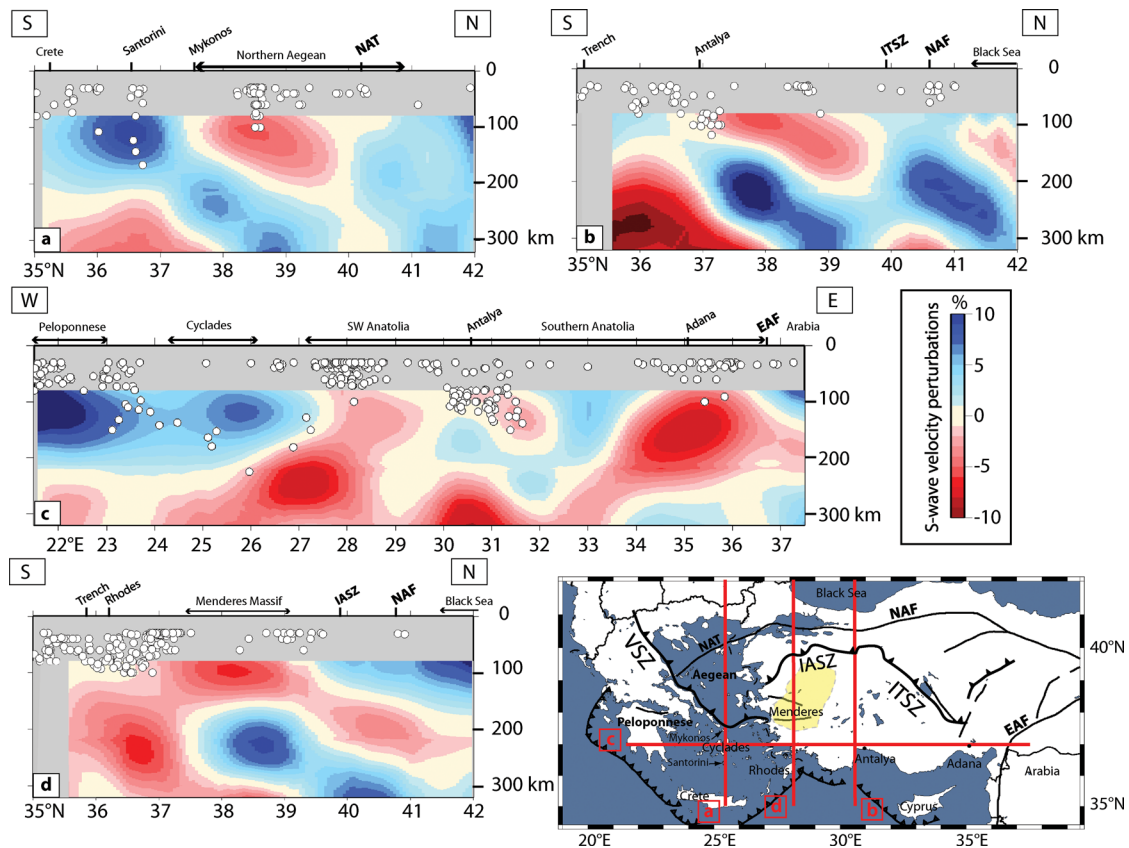


Figure 8. Selected vertical slices through our shear wave velocity perturbation model, showing perturbations with respect to the regionally averaged 1-D model (shown in Fig. 6b).

the structure is not surprising, given the complex tectonic history of the region, the strong deformation since the Cenozoic, and strong 3-D geometry of all major surface structures. The full exploration and interpretation of the 3-D model will be subject to further work while we here focus on some main features.

A main geodynamic question is whether the Hellenic slab continues uninterrupted beneath western Anatolia, the two parts possibly being separated by a slab tear. Govers & Wortel (2005) and Brun & Sokoutis (2010) argue that slab tear is requested beneath western Anatolia to allow for fast rollback of the Hellenic subduction. Fig. 8 shows four vertical profiles of relative velocity anomalies across different parts of the 3-D model. On Fig. 8(a), the Hellenic slab is clearly identified as a continuous high-velocity body, however with some horizontal smearing in its upper part due to the lack of stations and resolution in the southern Aegean. The apparent slab thickness is approximately 150 km; however the horizontal and vertical smoothing makes it impossible to give a precise estimate. Further east (Fig. 8b), beneath the region of Antalya, we again observe a northward-dipping high-velocity body which is well delineated by earthquake foci to 130 km depth. When its upper limit is extrapolated to the surface it outcrops in the vicinity of the Cyprus Trench. With these arguments at hand, we suggest that this high-velocity body can be identified as the Cyprus slab which has tentatively been identified by Biryol *et al.* (2011) as a subvertical high P -anomaly north of Cyprus at depths shallower than 200 km.

Fig. 8(c) shows a west–east cross-section where the high-velocity anomalies beneath the southern Aegean and southern Anatolia are clearly identified. They are separated by a strong low-velocity anomaly (see also Figs 7 and 8d) of significantly larger lateral extent

than the artificial anomaly modulations of Fig. 4(f) in the same area. We therefore interpret this well-resolved low-velocity anomaly as the trace of hot and buoyant asthenospheric mantle upwelling inside a slab tear between the western edge of the Cyprus slab and the eastern edge of the Hellenic slab. On an east–west cross-section similar in location to Fig. 8(c), de Boorder *et al.* (1998) documented a comparable but less striking feature at approximately the same location between 150 and 400 km depth in the EUR89B P -velocity model of Spakman *et al.* (1993). A low-velocity anomaly below western Anatolia also separates two high-velocity anomalies in horizontal slices at 100–200 km in model PM0.5 (Piromallo & Morelli 2003), however with a much broader north–south extension than in our model (see also Fig. 8d).

The second feature that we highlight here is the presence of high-velocity anomalies beneath most of Anatolia, north of what we identify as the Cyprus slab. These high-velocity anomalies can be identified in the depth slices of Fig. 7 at depths larger than or equal to 160 km. In well-oriented depth profiles as in Fig. 8(b) north of 40°N, these anomalies appear as dipping, continuous bodies, which are approximately 150 km thick. The striking resemblance to the Hellenic and to what we identify as the Cyprus slab leads us to tentatively interpret these structures as remnant slabs. In the cross-section of Fig. 8(b), the location of the northernmost high V_s anomaly beneath the Inner Tauride suture zone (ITSZ) may suggest a correspondence with the ancient (>60 Ma) subduction of a Neotethyan oceanic stripe along this suture (Pourtou *et al.* 2010). However, we checked that the extrapolation of the high V_s anomalies does not crosscut the surface along the suture outcrops (see, e.g. Fig. 8b).

Finally, we have no clear evidence of the NAF extending to lithospheric scale, as suggested by some authors (e.g. Armijo *et al.* 2002; Flerit *et al.* 2004; Laigle *et al.* 2008; Biryol *et al.* 2011) except for a small velocity contrast ($\sim 0.1 \text{ km s}^{-1}$) existing at 80 km depth between the northern and southern parts of the fault from the Marmara Sea to $\sim 35^\circ \text{E}$. We cannot exclude that the NAF extends below the crust, but either this extension is limited to depths shallower than $\sim 80 \text{ km}$ or the difference in velocity across it is negligible.

6 CONCLUSIONS

Our data set, composed of data from permanent and temporary seismic stations, yields an unprecedented data coverage for the entire Aegean-Anatolia region. With a 2-yr recording period, there are no major gaps in the azimuthal distribution of teleseismic events, and azimuthal weighting reduces the influence of the dominance of events located in the NE–SE quadrant. With this exceptional data set at hand, the 3-D model of V_s that we obtain from surface wave phase velocities has an almost uniform resolution across the whole study area. Due to trade-offs between crustal structure and uppermost mantle velocities, we consider the model resolved between 80 and 300 km depth. Our model varies smoothly with depth in the mantle to avoid non-resolved oscillations in the 3-D model. This means that thin ($< \sim 50 \text{ km}$ thick), anomalously high or low-velocity layers are not resolved.

The velocity distribution through our 3-D V_s model confirms previous findings that the mantle beneath the area is characterized by very low velocities between 80 and 200 km depth as compared to reference earth models. The presence of these low velocities favours that the lithosphere beneath the area is overall thin. An anomalously hot uppermost mantle could also explain the presence of a relatively high plateau in Anatolia. The lateral velocity variations are well resolved, and show details within the LVZ such as high-velocity structures beneath western and central Anatolia which we tentatively interpret as slab remnants. We interpret the southernmost one to be the Cyprus slab based on seismicity and spatial relationship with the Cyprus trench. The localized low velocities beneath SW Anatolia between this high-velocity body and the Hellenic slab is interpreted as a slab tear.

One important element to understand the dynamics of the Aegean-Anatolian region is numerical modelling of mantle processes. High-resolution seismic images provided by dense regional networks provide key input and working hypothesis for such modelling, and further work will be carried out to fully explore our 3-D model with this objective in mind.

ACKNOWLEDGMENTS

We are grateful to all participants in the field work and to Greek and Turkish colleagues for field work and access to data from the permanent broad-band networks. The data set was augmented with waveforms from the ORFEUS-VEBSN and IRIS-DMC facilities. We are indebted to V. Maupin for making her depth-inversion program available to us. Reviews by Associate Editor W. Friederich, E. Debayle and an anonymous reviewer greatly helped improving the manuscript. Most figures were created using the Generic Mapping Tools (Wessel & Smith 1991). The French national RESIF-SISMOB instrument pool made mobile seismic stations available for the field experiment. We also thank ISTERre and the Geology Laboratory of ENS Paris for providing supplementary instruments. Special thanks to H el ene Lyon Caen for participating in the station installation in

Bulgaria. The SIMBAAD project is funded by Agence Nationale de la Recherche under contract ANR-06-BLAN-0317.

REFERENCES

- Alvizuri, C. & Tanimoto, T., 2011. Azimuthal anisotropy from array analysis of Rayleigh waves in Southern California, *Geophys. J. Int.*, **186**, 1135–1151.
- Angus, D.A., Wilson, D.C., Sandvol, E. & Ni, J.F., 2006. Lithospheric structure of the Arabian and Eurasian collision zone in eastern Turkey from *S*-wave receiver functions, *Geophys. J. Int.*, **166**, 1335–1346.
- Armijo, R., Meyer, B., Navarro, S., King, G. & Barka, A., 2002. Asymmetric slip partitioning in the Sea of Marmara pull-apart: a clue to propagation processes of the North Anatolian Fault, *Terra Nova*, **14**, 80–86.
- Baumont, D., Paul, A., Zandt, G., Beck, S.L. & Pedersen, H., 2002. Lithospheric structure of the central Andes based on surface wave dispersion, *J. geophys. Res.*, **107**(B12), 2371, doi:10.1029/2001JB000345.
- B ecel, A. *et al.*, 2009. Moho crustal architecture and deep deformation under the North Marmara Trough, from the SEISMARMARA Leg 1 offshore-onshore reflection-refraction survey, *Tectonophysics*, **467**, 1–21.
- Beucler, E., Stutzmann, E. & Montagner, J.-P., 2003. Surface-wave higher mode phase velocity measurements using a roller coaster type algorithm, *Geophys. J. Int.*, **155**, 289–307.
- Bijwaard, H., Spakman, W. & Engdahl, E.R., 1998. Closing the gap between regional and global travel time tomography, *J. geophys. Res.*, **103**(B12), 30 055–30 078.
- Biryol, C.B., Beck, S.L., Zandt, G. &  zacar, A.A., 2011. Segmented African lithosphere beneath the Anatolian region inferred from teleseismic P-wave tomography, *Geophys. J. Int.*, **184**, 1037–1057.
- Bodin, T. & Maupin, V., 2008. Resolution potential of surface wave phase velocity measurements at small arrays, *Geophys. J. Int.*, **172**, 698–706.
- de Boor, C., 1978. A practical guide to splines, amplitude computation in heterogeneous media by ray perturbation theory: a finite element approach, *Geophys. J. Int.*, **103**, 341–354.
- de Boorder, H., Spakman, W., White, S.H. & Wortel, M.J.R., 1998. Late Cenozoic mineralization, orogenic collapse and slab detachment in the European Alpine Belt, *Earth planet. Sci. Lett.*, **164**, 569–575.
- Boschi, L., Ekstr om, G. & Kustowski, B., 2004. Multiple resolution surface wave tomography: the Mediterranean basin, *Geophys. J. Int.*, **157**, 293–304.
- Bourova, E., Kassaras, I., Pedersen, H.A., Yanovskaya, T., Hatzfeld, D. & Kiratzi, A., 2005. Constraints on absolute *S* velocities beneath the Aegean Sea from surface wave analysis, *Geophys. J. Int.*, **160**, 1006–1019.
- Brun, J.P. & Sokoutis, D., 2010. 45 m.y. of the Aegean crust and mantle flow driven by trench retreat, *Geology*, **38**, 815–818.
- Bruneton, M., Farra, V., Pedersen, H.A. & the SVEKALAPKO Seismic Tomography Working Group, 2002. Non-linear surface wave phase velocity inversion based on ray theory, *Geophys. J. Int.*, **151**, 583–596.
- Bruneton, M., Pedersen, H.A., Farra, V., Arndt, N.T., Vacher, P. & the SVEKALAPKO Seismic Tomography Working Group, 2004. Complex lithospheric structure under the central Baltic Shield from surface wave tomography, *J. geophys. Res.*, **109**, B10303, doi:10.1029/2003JB002947.
- Cambaz, M.D. & Karabulut, H., 2010. Love-wave group velocity maps of Turkey and surrounding regions, *Geophys. J. Int.*, **181**, 502–520.
- Chang, S.-J. *et al.*, 2010. Joint inversion for three-dimensional *s* velocity mantle structure along the Tethyan margin, *J. geophys. Res.*, **115**, B08309, doi:10.1029/2009JB007204.
- Chevrot, S. & Zhao, L., 2007. Multiscale finite-frequency Rayleigh wave tomography of the Kaapvaal craton, *Geophys. J. Int.*, **169**, 201–215.
- Cotte, N., Pedersen, H.A., Campillo, M., Farra, V. & Cansi, Y., 2000. Off-great circle propagation of intermediate period surface waves as observed on a dense array in the French Alps, *Geophys. J. Int.*, **142**, 825–840.
- Curtis, A., Trampert, J., Snieder, R. & Dost, B., 1998. Eurasian fundamental mode surface wave phase velocities and their relationship with tectonic structures, *J. geophys. Res.*, **103**(B11), 26 919–26 947.
- Debayle, E., 1999. SV-wave azimuthal anisotropy in the Australian upper mantle: preliminary results from automated Rayleigh waveform inversion, *Geophys. J. Int.*, **137**, 747–754.

- Debayle, E., Kennett, B. & Priestley, K., 2005. Global azimuthal seismic anisotropy and the unique plate-motion deformation of Australia, *Nature*, **433**, 509–512.
- Deschamps, G.A., 1972. Ray techniques in electromagnetic, *Proc. IEEE*, **60**, 1022–1035.
- Endrun, B., Meier, T., Lebedev, S., Bohnhoff, M., Stavrakakis, G. & Harjes, H.-P., 2008. *S* velocity structure and radial anisotropy in the Aegean region from surface wave dispersion, *Geophys. J. Int.*, **174**, 593–616.
- Erduran, M., Endrun, B. & Meier, T., 2008. Continental vs. oceanic lithosphere beneath the eastern Mediterranean Sea—implications from Rayleigh wave dispersion measurements, *Tectonophysics*, **457**, 42–52.
- Farra, V. & Madariaga, R., 1987. Seismic waveform modeling in heterogeneous media by ray perturbation theory, *J. geophys. Res.*, **92**, 2697–2712.
- Fichtner, A., Kennett, B.L.N., Igel, H. & Bunge, H.-P., 2008. Theoretical background for continental- and global-scale full-waveform inversion in the time-frequency domain, *Geophys. J. Int.*, **175**, 665–685.
- Flerit, F., Armijo, R., King, G. & Meyer, B., 2004. The mechanical interaction of the propagating North Anatolian Fault and the back-arc extension in the Aegean, *Earth planet. Sci. Lett.*, **224**, 347–362.
- Forsyth, D.W. & Li, A., 2005. Array-analysis of two-dimensional variations in surface wave velocity and azimuthal anisotropy in the presence of multipathing interference, in *Seismic Earth: Array Analysis of Broadband Seismograms*, Vol. 157, pp. 81–97, eds Levander, A. & Nolet, G., AGU Geophysical Monograph.
- Friederich, W., 1998. Wave-theoretical inversion of teleseismic surface waves in a regional network: phase velocity maps and a 3-D upper mantle shear wave velocity model for southern Germany, *Geophys. J. Int.*, **132**, 203–225.
- Friederich, W. & Wielandt, E., 1995. Interpretation of seismic surface waves in regional networks: joint estimation of wave-field geometry and local phase velocity. Method and numerical tests, *Geophys. J. Int.*, **112**, 264–275.
- Friederich, W., Wielandt, E. & Stange, S., 1994. Non-plane geometries of seismic surface wavefields and their implications for regional surface-wave tomography, *Geophys. J. Int.*, **119**, 931–948.
- Govers, R. & Wortel, W.J.R., 2005. Lithosphere tearing at STEP faults. Response to edges of subduction zones, *Earth planet. Sci. Lett.*, **236**, 505–523.
- Grad, M., Tiira, T., & ESC Working Group, 2009. The Moho depth map of the European Plate, *Geophys. J. Int.*, **176**, 279–292.
- Herrin, E. & Goforth, T., 1977. Phase-matched filters: Application to the study of Rayleigh waves, *Bull. seism. Soc. Am.*, **67**, 1259–1275.
- Hubans, F., 2010. Utilisation des corrélations de bruit micro-sismique pour l'analyse des propriétés du champ d'onde et l'imagerie crustale, *PhD thesis*, Joseph Fourier University, Grenoble, France.
- Karabulut, H., Paul, A., Afaçon Ergun, T., Hatzfeld, D., Childs, D.M. & Aktar, M., 2010. The lithospheric structure and upper mantle structure beneath the central Turkey obtained from receiver function profile, *Geophys. Res. Abstr.*, **12**, EGU2010-4225.
- Karagianni, E.E. & Papazachos, C.B., 2007. Shear velocity structure in the Aegean region obtained by joint inversion of Rayleigh and Love waves, *Geol. Soc. London, Spec. Publ.*, **291**, 159–181.
- Karagianni, E.E., Papazachos, C.B., Panagiotopoulos, D.G., Suhadolc, P., Vuan, A. & Panza, G.F., 2005. Shear velocity structure in the Aegean area obtained by inversion of Rayleigh waves, *Geophys. J. Int.*, **160**, 127–143.
- Kennett, B.L.N., Engdahl, E.R. & Buland, R., 1995. Constraints on seismic velocities in the Earth from traveltimes, *Geophys. J. Int.*, **122**, 108–124.
- Knapmeyer, M. & Harjes, H.-P., 2000. Imaging crustal discontinuities and the downgoing slab beneath western Crete, *Geophys. J. Int.*, **143**, 1–21.
- Kustowski, B., Ekström, G. & Dziewonski, A.M., 2008. The shear-wave velocity structure in the upper mantle beneath Eurasia, *Geophys. J. Int.*, **174**, 978–992.
- Laigle, M., Becel, A., de Voogd, B., Hirn, A., Taymaz, T., Ozalaybey, S. & Members of SEISMARMARA Leg1 Team, 2008. A first deep seismic survey in the Sea of Marmara: Deep basins and whole crust architecture and evolution, *Earth planet. Sci. Lett.*, **270**, 168–179.
- Lander, A.V. & Levshin, A.L., 1989. Recording, identification and measurement of surface wave parameters, in *Laterally Inhomogeneous Earth*, ed. Keilis-Borok, V.I., Kluwer, Dordrecht.
- Lebedev, S., Nolet, G., Meier, T. & van der Hilst, R.D., 2005. Automated multimode inversion of surface and s waveforms, *Geophys. J. Int.*, **162**, 951–964.
- Lévêque, J.-J., Rivera, L. & Wittlinger, G., 1993. On the use of the checkerboard test to assess the resolution of tomographic inversions, *Geophys. J. Int.*, **115**, 313–318.
- van der Lee, S. & Nolet, G., 1997. Upper mantle *s* velocity structure of North America, *J. geophys. Res.*, **102**, 22 815–22 838.
- Li, X. *et al.*, 2003. Receiver function study of the Hellenic subduction zone: imaging crustal thickness variations and the oceanic Moho of the descending African lithosphere, *Geophys. J. Int.*, **155**, 733–748.
- Lin, F.-C., Ritzwoller, M.H. & Snieder, R., 2009. Eikonal tomography: surface wave tomography by phase front tracking across a regional broadband seismic array, *Geophys. J. Int.*, **177**, 1091–1110.
- Maggi, A. & Priestley, K., 2005. Surface waveform tomography of the Turkish-Iranian plateau, *Geophys. J. Int.*, **160**, 1068–1080.
- Marone, F., van der Lee, S. & Giardini, D., 2004. Three-dimensional upper-mantle *S*-velocity model for Eurasia-Africa plate boundary region, *Geophys. J. Int.*, **158**, 109–130.
- Maupin V., 1988. Surface waves across 2D structures: a method based on coupled local modes, *Geophys. J. Int.*, **93**, 173–185.
- Maupin, V., 2011. Upper-mantle structure in southern Norway from beam-forming of Rayleigh wave data presenting multipathing, *Geophys. J. Int.*, **185**, 985–1002.
- Maupin, V. & Cara, M., 1992. Love-Rayleigh wave incompatibility and possible deep upper mantle anisotropy in the Iberian peninsula, *Pure appl. Geophys.*, **138**, 429–444.
- Mooney, W.D., Laske, G. & Masters, G., 1998. CRUST 5.1: a global crustal model at 5° × 5°, *J. geophys. Res.*, **103**, 727–747.
- Mutlu, A.K. & Karabulut, H., 2011. Anisotropic Pn tomography of Turkey and adjacent regions, *Geophys. J. Int.*, **187**, 1743–1758.
- Nolet, G., 1990. Partitioned waveform inversion and two-dimensional structure under the network of autonomously recording seismographs, *J. geophys. Res.*, **95**, 8499–8512.
- Papazachos, C. & Nolet, G., 1997. P and *s* deep velocity structure of the Hellenic area obtained by robust nonlinear inversion of travel times, *J. geophys. Res.*, **102**(B4), 8349–8367.
- Pedersen, H.A., 2006. Impacts of non-plane waves on two-station measurements of phase velocities, *Geophys. J. Int.*, **165**, 279–287.
- Pedersen, H.A., Coutant, O., Deschamps, A., Soulage, M. & Cotte, N., 2003. Measuring surface wave velocities beneath small broad-band arrays: test of an improved algorithm and application to the French Alps, *Geophys. J. Int.*, **154**, 903–912.
- Piomallo, C. & Morelli, A., 2003. P wave tomography of the mantle under the Alpine-Mediterranean area, *J. geophys. Res.*, **108**(B2), 2065, doi:10.1029/2002JB001757.
- Pollitz, F.F., 1999. Regional velocity structure in northern California from inversion of scattered seismic surface waves, *J. geophys. Res.*, **104**, 15 043–15 072.
- Pourteau, A., Candan, O. & Oberhänsli, R., 2010. High-pressure metasediments in central Turkey: constraints on the Neotethyan closure history, *Tectonics*, **29**, TC5004, doi:10.1029/2009TC002650.
- Sachpazi, M. *et al.*, 2007. Moho topography under central Greece and its compensation by Pn time-terms for the accurate location of hypocenters: the example of the Gulf of Corinth 1995 Aigion earthquake, *Tectonophysics*, **440**, 53–65.
- Saito, M., 1988. Disper 80: a subroutine package for the calculation of seismic modes solutions, in *Seismological Algorithms*, pp. 293–319, ed. Doornbos, D.J., Academic Press, San Diego, CA.
- Schivardi, R. & Morelli, A., 2011. EPmantle: a 3-D transversely isotropic model of the upper mantle under the European Plate, *Geophys. J. Int.*, **185**, 469–484.
- Sengör, A.M.C., Özeren, S., Genç, T. & Zor, E., 2003. East Anatolian high plateau as a mantle-supported, north-south shortened domal structure, *Geophys. Res. Lett.*, **30**(24), 8045, doi:10.1029/2009GL017858.

- Sniieder, R., 1988. Large-scale waveform inversion of surface waves for lateral heterogeneity, 1. Theory and numerical examples, *J. geophys. Res.*, **93**, 12 055–12 065.
- Sodoudi, F. *et al.*, 2006. Lithospheric structure of the Aegean obtained from P and s receiver functions, *J. geophys. Res.*, **111**, B12307, doi:10.1029/2005JB003932.
- Spakman, W., van der Lee, S. & van der Hilst, R.D., 1993. Travel-time tomography of the European-Mediterranean mantle down to 1400 km, *Phys. Earth planet. Int.*, **79**, 3–74.
- Suckale, J., Rondenay, S., Sachpazi, M., Charalampakis, M., Hosa, A. & Royden, L.H., 2009. High-resolution seismic imaging of the western Hellenic subduction zone using teleseismic scattered waves, *Geophys. J. Int.*, **178**, 775–791.
- Tarantola, A., 1987. *Inverse Problem Theory: Methods for Data Fitting and Parameter Estimation*, Elsevier, Amsterdam.
- Tarantola, A. & Valette, B., 1982. Generalized nonlinear inverse problems solved using the least square criterion, *Rev. Geophys.*, **20**, 219–232.
- Tesauro, M., Kaban, M.K. & Cloetingh, S.A.P.L., 2008. EuCRUST-07: a new reference model for the European crust, *Geophys. Res. Lett.*, **35**, L05313, doi:10.1029/2007GL032244.
- Tirel, C., Gueydan, F., Tiberi, C. & Brun, J.-P., 2004. Aegean crustal thickness inferred from gravity inversion. Geodynamical implications, *Earth planet. Sci. Lett.*, **228**, 267–280.
- Wessel, P. & Smith, W.H.F., 1991. Free software helps map and display data, *EOS, Trans. Am. geophys. Un.*, **72**, 441, 445–446.
- Wiener, N., 1949. *Time Series*, p. 163, MIT Press, Cambridge, MA.
- Yoshizawa, K. & Kennett, B.L.N., 2002. Non-linear waveform inversion for surface waves with a neighbourhood algorithm: application to multimode dispersion measurements, *Geophys. J. Int.*, **149**, 118–133.

SUPPORTING INFORMATION

Additional Supporting Information may be found in the online version of this article:

Figure S1. SUPPLEMENTARY RESOLUTION TESTS. (a) As in Fig. 4, the checkerboard test is carried out using an input model with 200-km anomalies. (b) The recovered model is calculated for the data (events and stations) distribution at 180 s period. Even if the total number of data is less than at 120 s period (Fig. 2b), the result is similar. The shape of anomalies is very well retrieved using azimuthal weighting and the amplitudes are only slightly damped ($\sim 0.03 \text{ km s}^{-1}$). (c) Input velocity model with a narrow (50–100 km

wide) high-velocity anomaly mimicking the slab, but slightly shifted southwards as compared to its expected location at $\sim 160 \text{ km}$ ($\lambda/3$) to test model recovery in areas with limited station coverage. The high-velocity anomaly is interrupted in SW Anatolia to test whether a slab tear beneath SW Anatolia can be detected. Overall, the output model (d) using the data distribution at 120 s period is reliable in locations with sufficient station coverage. Outside these areas, we observe erroneous geometries (e.g. the high velocity anomaly in the SE corner), smearing (between Crete and Cyprus) and amplitude reduction (e.g. between Crete and S Peloponnese). All these areas are excluded from the 3-D model as they are associated with high *a posteriori* errors on phase velocities.

Figure S2. HORIZONTAL SLICES AT SELECTED DEPTHS IN OUR 3-D SHEAR WAVE VELOCITY PERTURBATION MODEL. Lateral velocity changes are displayed as relative variations with respect to the average velocity at the given depth, shown in the lower left corner of each map. White circles are hypocentres from the 1998–2008 EMSC catalogue, which are located within 10 km of the section depth. Major sutures discussed in the text (from west to east: VSZ, Vardar suture zone; IASZ, Izmir-Ankara suture zone; ITSZ, Inner Tauride suture zone) are plotted as thick black lines.

Figure S3. DISTRIBUTION OF A POSTERIORI ERRORS ON V_s AT SELECTED DEPTHS. The error strongly increases between the 200 km and 250 km depth slice. However, it remains significantly smaller (less than $\sim 0.1 \text{ km s}^{-1}$) than the amplitudes of the retrieved anomalies (see Fig. 7).

Figure S4. HORIZONTAL SLICE AT 50 KM DEPTH IN OUR ABSOLUTE V_s MODEL. The colour scale is centred at 4.6 km s^{-1} , which would correspond to $V_p = 8 \text{ km s}^{-1}$ with a Poisson's ratio of 0.25. White circles are hypocentres from the 1998–2008 EMSC catalogue which are located within 2 km of the section depth. Caution must be taken in the interpretation of this map, as there may be a trade-off between crustal and uppermost mantle velocities during the inversion of the phase velocity dispersion curves for V_s .

Please note: Wiley-Blackwell are not responsible for the content or functionality of any supporting materials supplied by the authors. Any queries (other than missing material) should be directed to the corresponding author for the article.